Volume 1 | Number 1 | Jan 2013 | Pages 1–100

CrystEngComm

www.rsc.org/crystengcomm

ROYAL SOCIETY OF CHEMISTRY

ROYAL SOCIETY OF CHEMISTRY

www.rsc.org/crystengcomm

High Efficiency Photocatalytic Activity of Type-II SnO/Sn$_3$O$_4$ Heterostructures via Interfacial Charge Transfer

Weiwei Xia[*Ta], Haibo Wang[Ta], Xianghua Zeng[a*], Jie Han[b], Jun Zhu[a], Min Zhou[a], Shudong Wu[a]

[a] *College of Physics Science and Technology & Institute of Optoelectronic Technology ,Yangzhou University, Yangzhou 225002, P.R. China*

[b] *School of Chemistry and Chemical Engineering, Yangzhou University, Yangzhou 225002, P.R. China*

Abstract

Flower-like hollow microspheres were synthesized on a large scale using a one-step hydrothermal route. The as-prepared products were characterized by X-ray diffraction (XRD), scanning electron microscopy (SEM), high resolution transmission electron microscopy (HRTEM), X-ray photoelectron spectroscopy (XPS), and UV-vis diffuse reflectance spectroscopy. The results showed that the shells of the hollow microspheres were composed of numerous type-II SnO/Sn$_3$O$_4$ heterostructures. A 500 $^\circ$C annealing treatment changed the type-II SnO/Sn$_3$O$_4$ heterostructures into type-I SnO$_2$/Sn$_3$O$_4$ heterostructures; at 700 $^\circ$C, the products were pure SnO$_2$ semiconductors. A photocatalytic degradation test showed that the highest efficiency degradation of rhodamine B (RhB) was obtained using type-II SnO/Sn$_3$O$_4$ heterostructure semiconductors with a degradation rate constant of 2.3×10^{-3} min^{-1}. This highly efficient activity was induced by enhanced charge separation in type-II SnO/Sn$_3$O$_4$ heterostructure semiconductors.

Keywords: SnO/Sn$_3$O$_4$, SnO$_2$/Sn$_3$O$_4$, heterostructures, photocatalytic degradation

[*] *Corresponding authors; email: wwxia@yzu.edu.cn and xhzeng@yzu.edu.cn*
[Ŧ] *These authors contributed equally to this work.*

I. Introduction

In recent years, univalent tin oxides, such as SnO_2 and SnO, have attracted considerable interest as research subjects because of their wide ranging applications to lithium-ion batteries[1,2], sensitized solar cells[3,4], chemical and biological sensors[5,6] and photocatalysts[7,8,9,10]. In addition to univalent tin oxides, heterovalent tin oxides (e.g., Sn_3O_4, Sn_2O_3, and Sn_5O_6) with a variety of coordination structures have been a popular subject in both theoretical calculations and experimental studies on regulating the Sn(II)/Sn(IV) ratio[11,12]. Moreover, heterovalent tin structures have been reported to influence the physical properties of tin oxides. *Park et al.* found that heterovalent tin oxide exhibits more sensitivity for CH_2Cl_2 detection than either SnO or SnO_2 univalent oxides[13]. Theoretical calculations have confirmed that Sn_3O_4 has absorption bands that enable its use as a visible-light-driven photocatalyst for environmental remediation[14].

A univalent tin oxide-based composite, which includes SnO_2 and SnO, is a wide band gap semiconductor (SnO_2: $\simeq 3.5eV$, RT, SnO: $\simeq 2.7eV$, RT) and exhibits good activity and stability under irradiation in both acidic and basic media. However, there have been few reports on the direct use of pure tin oxide-based materials as photocatalysts, and it is well-known that SnO_2 exhibits low photocatalytic activity even under UV irradiation because of its its large band gap[15,16]. Currently, there are primarily two popular strategies that have been pursued in the literature to improve the photocatalytic activity of SnO_2. One strategy is to design various geometries and morphologies for tin oxide-based photocatalysis, because catalytic activity depends on the structural parameters of SnO_2 such as geometry, morphology, etc., and many complex nanostructures with novel geometry and morphology have been abundantly documented[17]. Among the aforementioned nanostructures, hollow structures of tin oxide-based architectures have also been extensively investigated for their large catalytically active surface area, high organic pollutant adsorption and the excellent incident light scattering within the structures[18]. Although considerable progress has been made in the synthesis of hollow spheres[19,20], it is still a major challenge to develop a facile route for the preparation of tin oxide hollow nanostructures with the desired optical properties, especially a one-step synthesis of a hollow structure. However, this strategy does not fundamentally solve

1   the problem of the fast recombination of photogenerated electron-hole pairs that hinder the

2   industrial application of photocatalytic techniques. Thus, minimizing the recombination of

3   photogenerated electron-hole pairs before they participate in redox processes is critical for

4   enhancing photocatalytic efficiency. A novel development has been the synthesis of tin

5   oxide-based photocatalysts using lower band gap semiconductors to form heterostructures

6   (e.g., SnO_2/TiO_2[21, 22], SnO_2/ZnO[23, 24], SnO_2/SnS_2[25], and SnO_2/Cd[26], $SnO_2–CdSe$[27]). Among

7   these heterostructures, type-II heterostructures are ideal for photocatalytic reactions in which

8   both rapid charge separation and low radiative recombination efficiency are required. The

9   improved photocatalytic activity of the hetero-junctions has also attributed to a large extent to

10   the enhanced separation of photo-induced electrons and holes via interfacial charge transfer.

11   Photocatalytic activity can be enhanced by the type-II heterostructures that are formed using

12   two types of semiconductors; however, the fabrication of these structures is complex because

13   two steps are usually required.

14   The close correlation between shape and morphology and the use of heterogeneous

15   photocatalysts makes the facile fabrication of desirable hollow nanoarchitectures of tin oxides

16   heterostructures a strongly desirable goal. Heterovalent tin oxides (e.g., Sn_3O_4, Sn_2O_3, and

17   Sn_5O_6) exhibit a narrower band gap than that of univalent tin oxides[28,29] and are thus

18   candidates for producing heterostructures of type-II univalent tin oxides. To the best of our

19   knowledge, this study is the first time that photocatalytic activity has been reported for

20   heterostructures of a homologous series of tin oxides. Herein, we report a simple one-step

21   hydrothermal route to fabricate SnO/Sn_3O_4 and SnO_2/Sn_3O_4 hetero-junctions for use as

22   photocatalysts. Heterostructures of homologous tin oxides exhibit excellent photocatalytic

23   performance. Notably, the annealing temperature can be simply tuned to easily control the

24   density of the heterostructures and the band structure of tin oxides, thereby improving the

25   optical properties of these materials. The heterostructures of tin oxides exhibit a much higher

26   efficiency than pure SnO_2 for the degradation of rhodamine B (RhB). Moreover, this simple

27   one-step hydrothermal route offers a wide range of practical applications and is a good

28   strategy for employing heterovalent tin oxide to fabricate a homologous series of tin oxides

29   for use as photocatalysts.

30

II. Experimental Section

The aforementioned heterostructure microspheres with hollow structures were prepared by a facile one step hydrothermal approach using sodium hydroxide, urea, and tin dichloride dehydrate ($SnCl_2 \cdot 2H_2O$) as precursors. In a typical synthesis, 60 ml of absolute ethanol and 140 ml of deionized water were mixed in a 250 ml beaker and stirred to ensure complete mixing. Then, 0.48 mM sodium hydroxide, 0.264 mM urea, and 0.04 mM tin dichloride dehydrate were dissolved in the mixture and agitated for approximately 1 h. The resulting mixture was transferred into a 200-ml sealed autoclave and heated in oven at 180 $^{\circ}$C for 18 h. The product was then centrifuged several times alternately in deionized water and ethanol, and the residual was dried for 10 h at 60 $^{\circ}$C in a vacuum stove. The final product was finally annealed at 300, 400, 500, 600 and 700 $^{\circ}$C for 2 h under atmosphere.

The morphologies of the obtained products were characterized using a field-emission scanning electron microscope (FESEM, s-4800II, Hitachi, 15kV). High resolution transmission electron microscopy (HRTEM) images and selective area electron diffraction (SAED) patterns were captured using a Tecanai G2 F30 S-Twin microscope at an accelerating voltage of 300 kV. Crystallographic data were obtained using power X-ray diffraction (Bruker, D8 Advance, Cu $k\alpha$ radiation, $\lambda = 1.5406$ Å). The phase composition of the as-prepared product was analyzed using an Axis Ultra X-ray photoelectron spectroscope (XPS, Kratos Analytical Ltd., UK) that was equipped with a standard monochromatic Al-$k\alpha$ source ($h\nu = 1486.6$ eV). The binding energy data were calibrated with respect to the C1s signal of the ambient hydrocarbons (C-H and C-C) at 284.8 eV. The absorption measurements were performed using a UV-vis-NIR spectrophotometer (UV-vis, Cary-5000, Varian) with an integrating sphere.

Photocatalytic experiments were conducted on the as-prepared samples to decompose or remove rhodamine B (RhB) aqueous solutions using the following procedure: 5 mg of the as-prepared samples were suspended in 25 ml of an aqueous solution of 1×10^{-5} mol/L RhB. Prior to irradiation, the suspensions were sonicated for 10 min and then magnetically stirred in the dark for 30 min to attain desorption-adsorption equilibrium. The solution was then exposed to UV irradiation from a mercury lamp (300 W) at room temperature. Five-milliliter

1 samples were collected every 30 min, centrifuged to remove the residual photocatalyst, and

2 the upper clear liquid was analyzed by recording the maximum absorption band (554 nm for

3 RhB) using a Shimadzu UV-3600 spectrophotometer. Also, 5 mg of commercial TiO_2 (P25)

4 was used in the control experiment. Additionally, the recycle experiments were performed for

5 five consecutive cycles with irradiation time of 150min under UV irradiation to test the

6 durability and irradiation time was kep

7 ## III. Results and Discussion
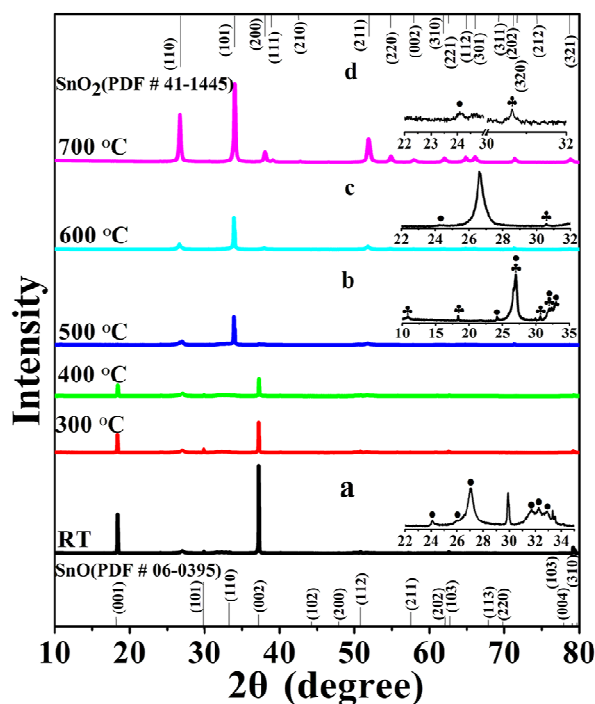
8

9 **Figure 1** XRD patterns of tin oxide-based powders before and after annealing at 300, 400, 500, 600,

10 and 700 °C for 2 h in air; insets show expanded powder XRD patterns of samples before and after

11 annealing at 500, 600, and 700 °C: inset (a) shows an enlarged spectrum, where peaks marked by (●)

12 correspond to Sn_3O_4 (JCPDS 16-0737); inset (b) shows an enlarged spectrum, where peaks marked by (♣)

13 correspond to other Sn_3O_4 phases (JCPDS 20-1293)

14 The XRD patterns of the as-prepared samples and the tin oxide-based powders formed at

15 varying oxidation temperatures of 300, 400, 500, 600, and 700 °C are shown in figure 1. The

16 as-prepared tin oxide-based powders that were annealed at temperatures of 300 and 400 °C

17 exhibited two sharp diffraction peaks corresponding to the reflections of a tetragonal SnO

18 phase (JCPDS 06-0395). A weak SnO peak was also observed at 29.989° (corresponding to

1   the (101) plane), indicating the simultaneous existence of the tetragonal SnO phase. Note that

2   extra peaks from minor phases could also be identified. The inset in figure 1a is an enlarged

3   spectrum over the $22°$ to $35°$ range. In addition to the SnO peaks, six characteristic peaks

4   could be identified (which are marked by (●)) as (101), $(\bar{1}20)$, (111), $(\bar{2}10)$, $(\bar{1}21)$, and

5   (210) reflections from Sn_3O_4 (JCPDS 16-0737). Following annealing above 400 $°C$, the

6   XRD spectra of samples changed dramatically. The peaks corresponding to SnO completely

7   disappeared at 500 $°C$, and new dominant peaks appeared that were indexed to the tetragonal

8   SnO_2 phase (JCPDS 41-1445), indicating the oxidation of SnO to SnO_2. The phase

9   transformation process is discussed later (see experimental details in †ESI, S1). Furthermore,

10 the intensities of the SnO_2 diffraction peaks increased with the annealing temperature. At 500

11 and 600 $°C$, two typical Sn_3O_4 peaks were simultaneously present. In the inset of figure 1(b),

12 the peaks marked by a (♣) were indexed to the (001), (100), (101), (111), (020), $(0\bar{2}1)$,

13 and $(\bar{1}12)$ reflections of Sn_3O_4 (JCPDS 20-1293). When the annealing temperature reached

14 700 $°C$, the products were transformed into pure rutile-structured SnO_2, which was confirmed

15 by fitting the SnO_2 peaks (JCPDS 41-445), as shown in the inset of figure 1 (d). Therefore, a

16 phase transition from SnO to SnO_2 occurred along with the formation of an intermediate

17 oxidation state of Sn_3O_4. The existence of Sn_3O_4 was confirmed by performing Raman

18 spectroscopy to clarify the crystalline compositions and structures of the aforementioned

19 samples (see experimental details in †ESI, S2).
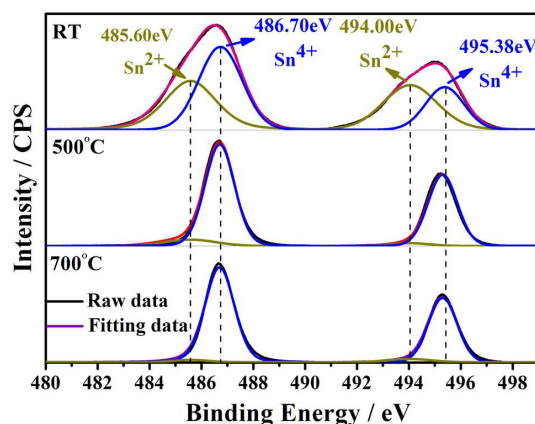
20

21 **Figure 2** XPS spectra of Sn 3d for tin oxide-based powders before and after annealing at 500 and 700 $°C$
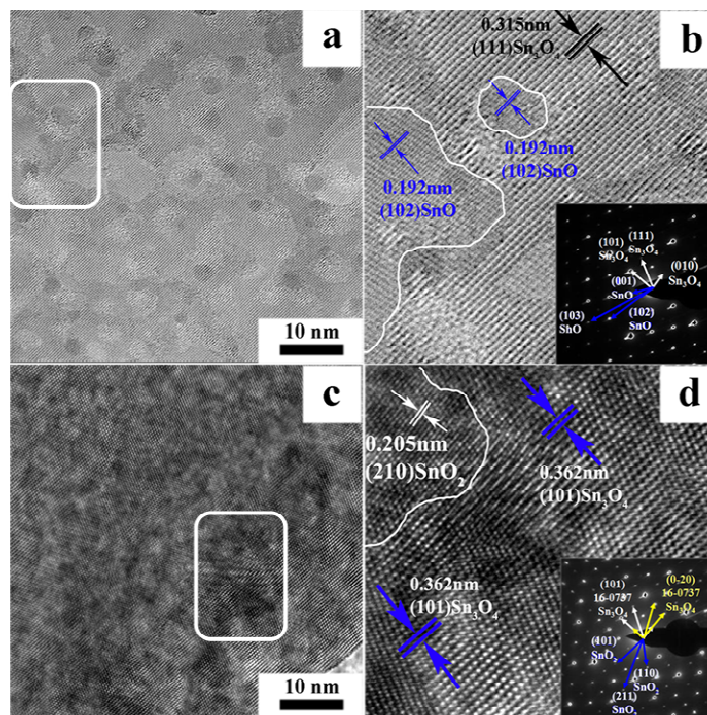22 for 2 h in air

1   To gain insight into the evolution of the tin oxide during the annealing process, X-ray

2   photoelectron spectra (XPS) was performed to investigate the changes in the Sn-related states

3   under different annealing temperatures (see figure 2). The Sn 3d spectrum exhibited spin-orbit

4   doublet peaks at $\simeq$486 eV (Sn^{2+} $3d_{5/2}$) and $\simeq$495 eV (Sn^{2+} $3d_{3/2}$). After annealing above

5   500 $^{\circ}$C, the main peaks shifted to higher binding energies, which matched the binding energies

6   of Sn^{4+} (at 486.7 eV and 495.4 eV for $3d_{5/2}$ and $3d_{3/2}$, respectively) well, and the Sn^{4+} content

7   increased and gradually dominated the material composition. The binding energies of the

8   Sn-related states obtained in this experiment were consistent with the XRD results.
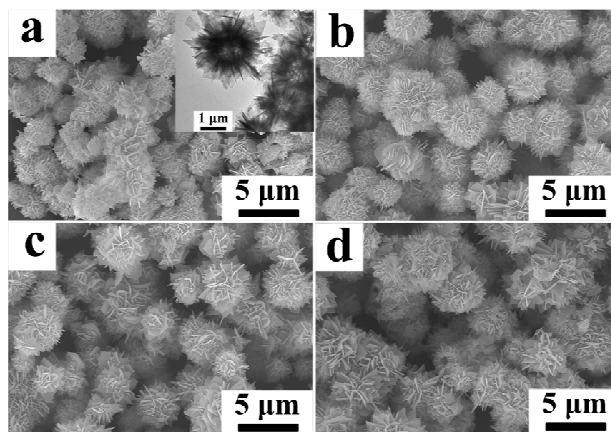
9

10   **Figure 3** SEM images of tin oxide-based microspheres (a) before and after annealing at (b) 300, (c) 500,
11   and (d) 700 $^{\circ}$C for 2 h in air; inset in (a) is a TEM image of the as-synthesized tin oxide microspheres

12   The product morphologies were studied by SEM. Figure 3 shows typical SEM images of

13   the collected tin oxide microspheres before and after annealing treatments at different

14   temperatures. Three-dimensional (3D) microspheres assembled into sheet-like subunits with

15   diameters ranging from 3 to 5 μm. TEM measurements were performed to characterize the

16   sample structures further and are shown in the inset of figure 3 (a). The obvious contrast

17   between the dark edges and the pale centers confirms that these microspheres were hollow. It

18   has been reported that this hollow structure can improve light harvesting through multiple

19   light reflections and scattering effects that can be used for applications in the

20   photo-decomposition of organic compounds. Furthermore, the morphology of the hollow

1   microsphere structures was faithfully preserved during the calcination process. Therefore,

2   hollow microspheres can be synthesized on a large scale, where the shells of the microspheres

3   are covered with numerous nanoflakes.

4

5   **Figure 4** HRTEM images and SAED patterns of as-synthesized tin oxide-based heterostructures;
6   lattice-resolved HRTEM images were taken from the edge of the microspheres obtained (a) before and (b)
7   after annealing at 500 $^{\circ}$C for 2 h in air; insets show corresponding SAED patterns

8   To obtain detailed information about the microstructure of the as-synthesized tin

9   oxide-based microspheres, HRTEM observations and selected-area electron diffraction

10   (SAED) analysis were carried out: the results are shown in figure 4. The SAED patterns in the

11   insets of figure 4 show two different types of crystal phases in the samples: both phases of the

12   heterostructures were crystalline. Meanwhile, the HRTEM images of the region that are

13   marked by a white line confirmed the presence of crystalline SnO/Sn_3O_4 and SnO_2/Sn_3O_4

14   crystal lattices in the interfacial region, as shown in figure 4. The HRTEM images also clearly

15   revealed the in situ formation of heterostructures within the interface, which would have

16   facilitated interfacial electron transfer and accordingly increased the photocatalytic activity.

17   The aforementioned analysis confirmed that SnO/Sn_3O_4 and SnO_2/Sn_3O_4 composites with

18   heterostructures formed in our prepared samples. Note that the SnO content in the SnO/Sn_3O_4

1   semiconductors disappeared as the annealing temperature increased until finally, only SnO_2

2   was observed at 700 $^{\circ}$C; thus, the annealing temperature could be tuned to adjust the tin oxides

3   constituents to produce the required optical properties.

4   Typical UV-vis spectroscopy measurements were used to further confirm the formation of

5   the heterostructures. In the literature[30, 31], SnO_2 has been reported to be a direct band gap

6   material, and SnO and Sn_3O_4 have been reported to be indirect band gap materials: the optical

7   band gap energy (E_g) of these materials can be calculated using the equation given below[32],

8    $$\alpha h\nu = C(h\nu - E_g)^n,$$

9   where n is equal to 1/2 and 2 for direct allowed transitions and indirect transitions,

10   respectively.
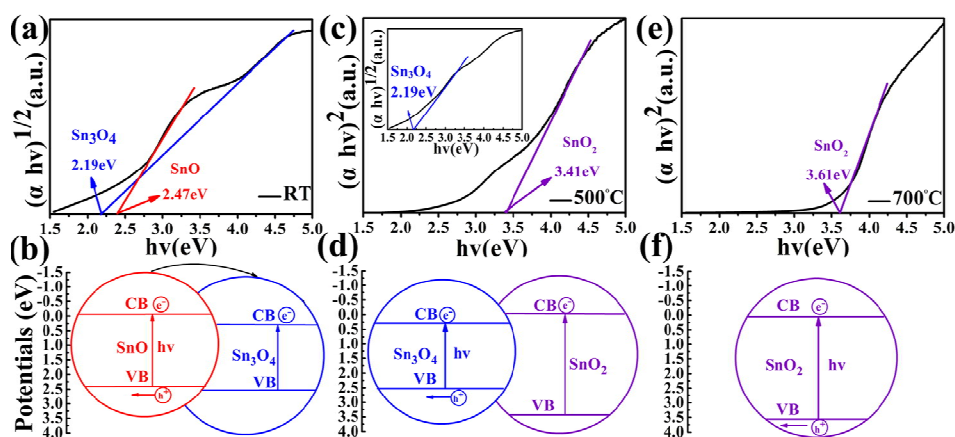
11

12   **Figure 5** Plots of $(\alpha h\nu)^{n/2}$ vs. photon energy $(h\nu)$ for (a) as-prepared tin oxide-based

13   heterostructures and heterostructures formed at oxidation temperatures of (c) 500 and (e) 700 $^{\circ}$C; (b), (d)

14   and (f) are the corresponding schematic diagrams of the energy band structures of tin oxide-based

15   heterostructures

16   The spectra of the SnO/Sn_3O_4 and SnO_2/Sn_3O_4 heterostructures are plotted in figure 5 (a

17   and c): two slopes can be clearly observed that indicate the formation of heterostructures. The

18   E_g values of SnO and Sn_3O_4 in the SnO/Sn_3O_4 heterostructures were evaluated as 2.47 and

19   2.19 eV, respectively. Upon heating to 500 $^{\circ}$C, the E_g values for SnO_2 and Sn_3O_4 in the

20   SnO_2 /Sn_3O_4 heterostructures were evaluated as 3.41 and 2.19 eV, respectively. Meanwhile,

21   further increasing the annealing temperature to 700 $^{\circ}$C yielded only one slope in figure 5(e),

1   and the E_g was estimated at 3.61 eV, which was in agreement with the reported value for

2   SnO_2 (3.5-3.7 eV). The valence band edge positions of the tin oxide-based heterostructures

3   were estimated using electronegativity concepts. The valence band potentials of a

4   semiconductor at the point of zero charge can be calculated using the following empirical

5   equation[33, 34, 35]:

6    $$E_{VB} = X - E^e + 0.5E_g \qquad\qquad (1),$$

7   where E_{VB} is the VB edge potential, and X is the electronegativity of the semiconductor,

8   which is the geometric mean of the electronegativity of the constituent atoms. The X values

9   for SnO, SnO_2 and Sn_3O_4 are 5.68, 6.24 and 5.91 eV, respectively. The energy of the free

10   electrons on the hydrogen scale is denoted by E^e ($\simeq 4.5$ eV), E_g is the band gap energy of

11   the semiconductor, and E_{CB} can be determined from $E_{CB} = E_{VB} - E_g$. Figure 5 (b, d, and f)

12   shows the schematic diagrams of the energy band structures of the tin oxide-based

13   heterostructures. Sn_3O_4 exhibited a narrower band gap than the band energy alignment of SnO

14   and SnO_2, and the valence and conduction band alignments for Sn_3O_4 were staggered relative

15   to those of SnO and SnO_2; therefore SnO/Sn_3O_4 was a type-II heterostructure. In SnO_2/Sn_3O_4,

16   the band gap Sn_3O_4 was embedded in that of SnO_2; thus, SnO_2/Sn_3O_4 was a type-I

17   heterostructure.
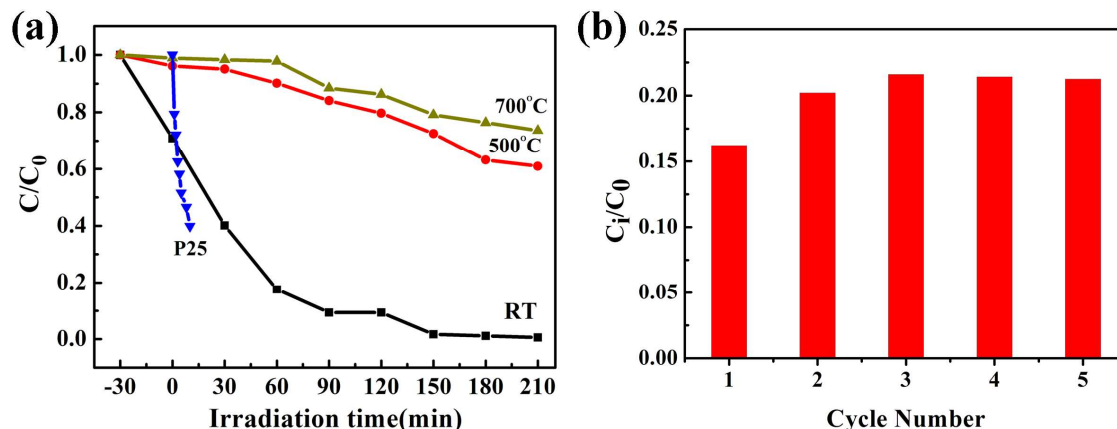
19   **Figure 6** (a) Comparison of photocatalytic degradation of RhB in the presence of tin oxide-based
20   heterostructures; (b) Cycling runs for the photocatalytic degradation of RhB over SnO/Sn_3O_4 under UV
21   irradiation

1   The photocatalytic activities of the as-synthesized different heterostructures were

2   evaluated by the degradation of a RhB dye in water under UV light irradiation, as shown in

3   figure 6(a). Figure 6(a) shows the absorption spectra of the RhB solution in the presence of tin

4   oxide-based semiconductors. Figure 6(a) shows that the tin oxide-based heterostructures

5   SnO/Sn_3O_4 and SnO_2/Sn_3O_4 exhibited a better catalytic degradation than SnO_2, whereas the

6   SnO/Sn_3O_4 heterostructure semiconductors performed the most efficient degradation of RhB.

7   The poor performance of SnO_2 semiconductors could be attributed to the low negative

8   conduction potential of SnO_2, because the conduction band bottom potential of SnO_2 is near

9   that of O_2/O^{2-} (−0.046 eV vs. SHE), indicating that SnO_2 readily undergoes photocorrosion in

10   aqueous media containing oxygen and that the over potential is too small to reduce O_2 with

11   photoexcited electrons[36]; therefore, photocatalytic degradation using SnO_2 was not effective.

12   For practical photocatalytic applications, the recycling of photocatalyst is very important. In

13   the durability tests, SnO/Sn_3O_4 was repeatedly used for the RhB photodegradation reaction 5

14   times (Figure 6 (b)). The experimental results indicated that no apparent deactivation of

15   photocatalyst is seen after 5 cycles as compared to the fresh catalyst.

16   Catalytic degradations of dye have been reported in the literature[37, 38]. For SnO/Sn_3O_4 with

17   a type-II heterostructure, electrons could be excited from the valence bands to the conduction

18   bands of SnO semiconductors by UV irradiation because of the band offset: the generated

19   electrons on the conduction band of SnO were directly injected into the conduction band of

20   Sn_3O_4, whereas the holes remained on the valence band (as shown in Fig. 5b). Thus, more

21   electrons accumulated in the conduction band of the SnO, resulting in more holes in the

22   valence band of SnO, i.e., interfacial charge separation occurred. The electrons that were

23   eventually localized in the conduction band of Sn_3O_4 reduced O_2 to form superoxide ions

24   $*O_2^-$, and the holes located in the valence band of SnO reacted with the hydroxyl group to

25   produce the hydroxyl radicals (*OH) that degraded RhB in the photoreaction. The high

26   efficient photodegradation activity of SnO/Sn_3O_4 can be explained as, on the one hand, the

27   morphology of SnO/Sn_3O_4 exhibits a high surface-to-volume ratio, which is benefit to the

28   adsorption of dye RhB molecules, the photodegradation efficiency will improve; on the other

29   hand, the life span of photogenerated electron-hole pair is large enough to migrate and is

30   available for redox reactions at photocatalyst surface, as the recombination rate of the electron

1 and hole excited from indirect semiconductor SnO is lower than that of the direct

2 semiconductor, which will be favorable for the charge separation. Therefore, the samples

3 SnO/Sn_3O_4 prepared at room temperature show a high efficient photodegradation activity, as

4 shown in Figure 6.

5 For the type-I SnO_2/Sn_3O_4 heterostructure, electrons were excited upon light irradiation of

6 both the SnO_2 and Sn_3O_4 semiconductors. Then, unlike in the type-II heterostructures, more

7 electrons and holes recombined while electrons and holes were produced for both the SnO_2

8 and Sn_3O_4 semiconductors, resulting in a photocorrosion effect as the electrons and holes

9 recombined in the conduction and valence bands of SnO_2 and Sn_3O_4. Sn_3O_4 is an indirect

10 semiconductor; therefore, the recombination rate of the indirect semiconductor was relatively

11 lower, and some electrons and holes participated in the photocatalytic degradation of RhB

12 before recombination, which explains why the type-I SnO_2/Sn_3O_4 heterostructure had a much

13 higher photocatalytic degradation effect than the SnO_2 semiconductor. The degradation

14 efficiency of a photocatalyst can be defined as follows[39]:

15
$$Degradation(\%) = (1 - C/C_0) \times 100\% \qquad (2),$$

16 where C_0 is the RhB concentration at equilibrium adsorption, and C is the residual

17 concentration of RhB at different illumination intervals. The photodegradation of RhB

18 follows pseudo-first-order kinetics, which can be expressed as follows:

19
$$\ln(C/C_0) = -kt \qquad (3),$$

20 where k (min^{-1}) is the degradation rate constant. Equation (3) was used to calculate the

21 degradation rate constants of 2.3×10^{-3} and $3.6 \times 10^{-5}\,min^{-1}$ for the SnO/Sn_3O_4 and SnO_2/Sn_3O_4

22 semiconductors, respectively. Although the degradation rate constant for SnO/Sn_3O_4 is much

23 smaller than the P25 (9.2×10^{-2}). We believe that our report provides a new approach to

24 realize high Efficiency Photocatalytic of heterostructures of type-II univalent tin oxides.

25 Therefore, enhanced photocatalytic degradation of RhB solutions was observed using

26 SnO/Sn_3O_4 with type-II heterostructures as photocatalysts, as shown in Figure 6. The

27 observed phenomenon was consistent with other reports.[40] Furthermore, the flower-like

1   hollow microspheres is still inherited after five consecutive cycles (See Figure S3 in the

2   supporting Information).

3

4

5 IV. Conclusions

6   In summary, tin oxide semiconductors with a morphology of flower-like hollow

7   microspheres were synthesized using a one-step hydrothermal route and a series of annealing

8   processes. The as-prepared products were characterized by XRD, scanning electron

9   microscopy (SEM), high resolution transmission electron microscopy (HRTEM), X-ray

10   photoelectron spectroscopy (XPS), and UV-vis diffuse reflectance spectra. Systematic

11   measurements revealed that the as-prepared flower-like hollow microspheres had a type-II

12   SnO/Sn_3O_4 heterostructure. After a 500 $^{\circ}$C annealing treatment, the original SnO/Sn_3O_4

13   heterostructure changed into SnO_2/Sn_3O_4 with a type-I heterostructure, and the products were

14   SnO_2 at 700 $^{\circ}$C. The original prepared SnO/Sn_3O_4 semiconductors with type-II heterostructures

15   performed the highest efficiency degradation of rhodamine B (RhB) with a degradation rate

16   constant of $2.3 \times 10^{-3} \, min^{-1}$. This highly efficient activity was induced by the enhanced charge

17   separation in the SnO/Sn_3O_4 semiconductors with type-II heterostructure. This typical hollow

18   structure has two advantages for photocatalytic activity: the structure has a high

19   surface-to-volume ratio, which enables multi-reflections of irradiated light within the interior

20   cavities, and the products consist of two phases of homologous tin oxides. We believe that our

21   prepared SnO/Sn_3O_4 and SnO_2/Sn_3O_4 heterostructures microspheres can be used as

22   visible-light-driven high-performance photocatalysts. Studies on such applications are

23   currently underway.

1   Jiangsu Higher Education Institutions. We would also like to acknowledge technical support

2   from the Testing Center of Yangzhou University.

3

4

5   **References**

[1] P. Meduri, C. Pendyala, V. Kumar, G. U. Sumanasekera, M. K. Sunkara, Nano Lett. 2009, 9 (2), 612.

[2] Z. Y. Wang, D. Y. Luan, X. W. Lou, J. Am. Chem. Soc. 2011, 133 (13), 4738.

[3] H. J. Snaith, C. Ducati, Nano Lett. 2010, 10 (4), 1259.

[4] M. A. Hossain, G. W. Yang, M. Parameswaran, J. R. Jennings, Q. J. Wang, J. Phys. Chem. C, 2010, 114 (49), 21878 .

[5] J. T. McCue, J. Y. Ying, Chem. Mater. 2007, 19 (5), 1009.

[6] J. Huang, N. Matsunaga, J. Shimanoe, N. Yamazoe, T. Kunitake, Chem. Mater. 2005, 17 (13), 3513.

[7] L. R. Zheng, Y. H. Zheng, C. Q. Chen, J. F. Zhu, Inorg. Chem. 2009, 48 (5), 1819.

[8] Y. C. Zhang, Z. N. Du, D. D. Dionysiou, ACS Appl. Mater. Interfaces. 2011, 3(5), 1528.

[9] C. M. Fan, Y. Peng, Q. Zhu, A. W. Xu, J. Phys. Chem. C. 2013, 117 (46), 24157.

[10] A. K. Sinha, P. K. Manna, M. Pradhan, Chem. Commun. 2014, 50, 2847.

[11] A. Seko, A. Togo, I. Tanaka, Phys. Rev. Lett. 2008, 100, 45702.

[12] M. S. Moreno, R. F. Egerton, P. A. Midgley, Phys. Rev. B. 2004, 69, 041307.

[13] S. H. Park, Y. C. Son, W. S. Willis, S. L. Suib, K. E. Creasy, Chem. Mater. 1998, 10 (9), 2389.

[14] O. M. Berengue, R. A. Simon, A. J. Chiquito, J. Appl. Phys. 2010, 107, 033717.

[15] H. J. Wang, F. Q. Sun, Y. Zhang, J. Mater. Chem. 2010, 20, 5641.

[16] C. Nasr, P.V. Kamat, S. Hotchandani, Journal of Electroanalytical Chemistry. 1997, 420, 201.

[17] S. W. Liu, G. C. Huang, J. G. Yu, P. K. Wong, ACS Appl. Mater. Interfaces. 2014, 6 (4), 2407.

[18] H. J. You, R. Liu, C. C. Liang, B. J. Ding, J. Mater. Chem. A. 2013, 1, 4097.

[19] L. Xu, M. P. Steinmiller, S. E. Skrabalak, J. Phys. Chem. C. 2012, 116 (24), 871.

[20] M. T. Niu, F. Huang, L. F. Cui, Y. S. Wang, ACS Nano, 2010, 4 (2), 681.

[21] K. Vinodgopal, I. Bedja, P. V. Kamat, Chem. Mater. 1996, 8 (8), 2180.

[22] Z. Y. Liu, D. D. Sun, P. Guo, J. O. Leckie, Nano Lett. 2007, 7 (4), 1081.

[23] M. T. Uddin, Y. Nicolas, C. Olivier, T. Toupance, L. Servant, M. M. Muller, H. J. Kleebe, J. Ziegler, W. Jaegermann, Inorg. Chem. 2012, 51 (14), 7764.

[24] J. S. Lee, O. S. Kwon, J. Jang, J. Mater. Chem. 2012, 22, 14565.

[25] Y. C. Zhang, Z. N. Du, K. W. Li, M. Zhang, D. D. Dionysiou, ACS Appl. Mater. Inter. 2011, 3, 1528.

[26] A. Kar, S. Kundu, A. Patra, RSC Adv. 2012, 2, 10222.

[27] C. Nasr, P.V. Kamat, S. Hotchandani, Journal of Electroanalytical Chemistry. 1997, 420, 201.

[28] F. P. Wang, X. T. Zhou, J. G. Zhou, T. K. Sham, J. Phys. Chem. C. 2007, 111 (51), 18839.

[29] Y. H. He, D. Z. Li, J. Chen, Y. Shao, J. J. Xian, RSC Adv. 2014, 4, 1266.

[30] M. Losurdo, D. Barreca, P. Capezzuto, G. Bruno, E. Tondello, Surface and Coatings Technology. 2002, 151, 2.

[31] F. Demichelis, V. Smurro, A. Tagliaferro, E. Tresso, Journal of Physics D: Applied Physics. 1985, 18, 1825.

[32] H. Deng, J. M. Hossenlopp, Journal of Physical Chemistry B. 2005, 109 (1), 66.

[33] M. A. Butler, D. S. Ginley, J. Electrochem. Soc. 1978, 125 (2), 228 (1978).

[34] X. Lin, J. Xing, W. Wang, Z. Shan, F. Xu, F. Huang, J. Phys. Chem. C. 2007, 111 (49), 18288.

[35] X. Zhang, L. Zhang, T. Xie, D. Wang, J. Phys. Chem. C. 2009, 113 (17), 7371.

[36] X. Xu, R. Lu, X. Zhao, S. Xu, X. Lei, F. Zhang, D.G. Evans, Appl. Catal. B. 2011, 102, 147.

[37] R. M. Navarro, F. D. Valle, J. A. V. de la Mano, Advances in Chemical Engineering. 2009, 36, 111.

[38] H. H. Mohamed, D. W. Bahnemann, Applied Catalysis B: Environmental. 2012, 128, 91.

[39] V. Taghvaei, A. Habibi-Yangjeh, M. Behboudnia, Physica E. 2010, 42 (7), 1973.

[40] X. M. Xiang, L. J. Chou, X. H. Li, Phys. Chem. Chem. Phys. 2013, 15, 19545.